© 2019. Published by The Company of Biologists Ltd | Development (2019) 146, dev174029. doi:10.1242/dev.174029

TECHNIQUES AND RESOURCES

RESEARCH ARTICLE

A high-content imaging approach to profile *C. elegans* embryonic development

Shaohe Wang[1,2,*,], Stacy D. Ochoa[1,‡,**], Renat N. Khaliullin[1,§,**], Adina Gerson-Gurwitz[1,¶], Jeffrey M. Hendel[1], Zhiling Zhao[1], Ronald Biggs[1], Andrew D. Chisholm[3], Arshad Desai[1], Karen Oegema[1,‡‡] and Rebecca A. Green[1,‡‡]**

ABSTRACT

The *Caenorhabditis elegans* embryo is an important model for analyzing mechanisms of cell fate specification and tissue morphogenesis. Sophisticated lineage-tracing approaches for analyzing embryogenesis have been developed but are labor intensive and do not naturally integrate morphogenetic readouts. To enable the rapid classification of developmental phenotypes, we developed a high-content method that employs two custom strains: a Germ Layer strain that expresses nuclear markers in the ectoderm, mesoderm and endoderm/pharynx; and a Morphogenesis strain that expresses markers labeling epidermal cell junctions and the neuronal cell surface. We describe a procedure that allows simultaneous live imaging of development in 80-100 embryos and provide a custom program that generates cropped, oriented image stacks of individual embryos to facilitate analysis. We demonstrate the utility of our method by perturbing 40 previously characterized developmental genes in variants of the two strains containing RNAi-sensitizing mutations. The resulting datasets yielded distinct, reproducible signature phenotypes for a broad spectrum of genes that are involved in cell fate specification and morphogenesis. In addition, our analysis provides new *in vivo* evidence for MBK-2 function in mesoderm fate specification and LET-381 function in elongation.

KEY WORDS: High-content imaging, Embryogenesis, *C. elegans*, Morphogenesis, Cell fate specification

INTRODUCTION

The *Caenorhabditis elegans* embryo is an important model for studying cell fate specification and morphogenesis (Armenti and Nance, 2012; Chisholm and Hsiao, 2012; Jackson and Eisenmann, 2012; Lamkin and Heiman, 2017; Loveless and Hardin, 2012; Priess, 2005; Spickard et al., 2018; Vuong-Brender et al., 2016; Wang and Seydoux, 2013). *C. elegans* embryonic development occurs in two phases (Fig. 1A). During the 6 h following fertilization, ten rounds of cell division coupled to cell fate specification generate the three germ layers (ectoderm, mesoderm, and endoderm; Sulston et al., 1983); the subsequent 7 h are largely post-mitotic and consist of morphogenetic events that structure the differentiated tissues (Chisholm and Hardin, 2005; Vuong-Brender et al., 2016).

In a pioneering study, the invariant lineage of the embryo was manually determined by differential interference contrast microscopy (Sulston et al., 1983). Subsequent work involving the imaging fluorescent histones enabled semi-automated tracking of nuclei through the first nine to ten rounds of cell division (Bao et al., 2006; Giurumescu et al., 2012; Santella et al., 2010). Newer methods have combined histone-based lineage tracing with monitoring of specific markers to assess the outcome of cell fate decisions (Du et al., 2015, 2014; Ho et al., 2015; Murray et al., 2008, 2012). In one recent approach, the fate of cells in the 13-cell-stage embryo was uniquely barcoded by monitoring the combinatorial expression of lineage-specific markers among their progeny five cell divisions later (Du et al., 2015, 2014). Although approaches based on lineage tracing are very powerful, they also have limitations. In particular, they are labor intensive, require expertise beyond that available in the majority of labs and are relatively low throughput, which limits their utility for larger-scale screening efforts. Extending lineage tracing to inform on morphogenetic events during the second half of embryogenesis has also been challenging (Christensen et al., 2015).

Here, we describe a technically straightforward method that complements existing approaches to enable rapid profiling of a broad spectrum of developmental processes during embryogenesis. The method is based on a pair of custom-engineered strains: a Germ Layer strain that expresses nuclear markers in the ectoderm, mesoderm and endoderm/pharynx, and a Morphogenesis strain that labels epidermal cell junctions and the neuronal cell surface. We describe a filming procedure that allows the simultaneous monitoring of 80-100 embryos in 3D at 20-min time resolution and provide user-friendly custom software that locates individual embryos within a larger field, to generate cropped, oriented image stacks; we further provide a FIJI script that compiles the cropped sequences into composite 4D movies. We demonstrate the utility of our approach by characterizing the knockdown phenotypes of 40 previously characterized developmental genes. Manual scoring revealed that our method generates reproducible and informative phenotypic signatures that enable the functional classification of genes that are involved in a broad spectrum of developmental processes. We also uncovered previously unreported functions for two genes in the 40-gene set. Specifically, our approach provided *in vivo* evidence that MBK-2 acts in anterior fate specification and that LET-381 acts in the late stages of embryo elongation.

[1]Ludwig Institute for Cancer Research, Department of Cellular and Molecular Medicine, University of California San Diego, La Jolla, CA 92093, USA. [2]Biomedical Sciences Graduate Program, University of California, San Diego, La Jolla, CA 92093, USA. [3]Section of Cell and Developmental Biology, Division of Biological Sciences, University of California, San Diego, La Jolla, CA 92093, USA.
*Present address: Cell Biology Section, National Institute of Dental and Craniofacial Research, National Institutes of Health, Bethesda, MD 20892, USA. ‡Present address: Department of Biology, San Diego State University, San Diego, CA 92182, USA. §Present address: Recursion Pharmaceuticals, Salt Lake City, UT 84101, USA. ¶Present address: Small Molecule Discovery Program, Ludwig Institute for Cancer Research, La Jolla, CA 92093, USA.

**These authors contributed equally to this work

‡‡Authors for correspondence (koegema@ucsd.edu; regreen@ucsd.edu)

S.W., 0000-0001-9522-2359; S.D.O., 0000-0001-8484-8321; A.D., 0000-0002-5410-1830; K.O., 0000-0001-8515-7514

Received 26 November 2018; Accepted 11 March 2019

Development (2019) 146, dev174029. doi:10.1242/dev.174029

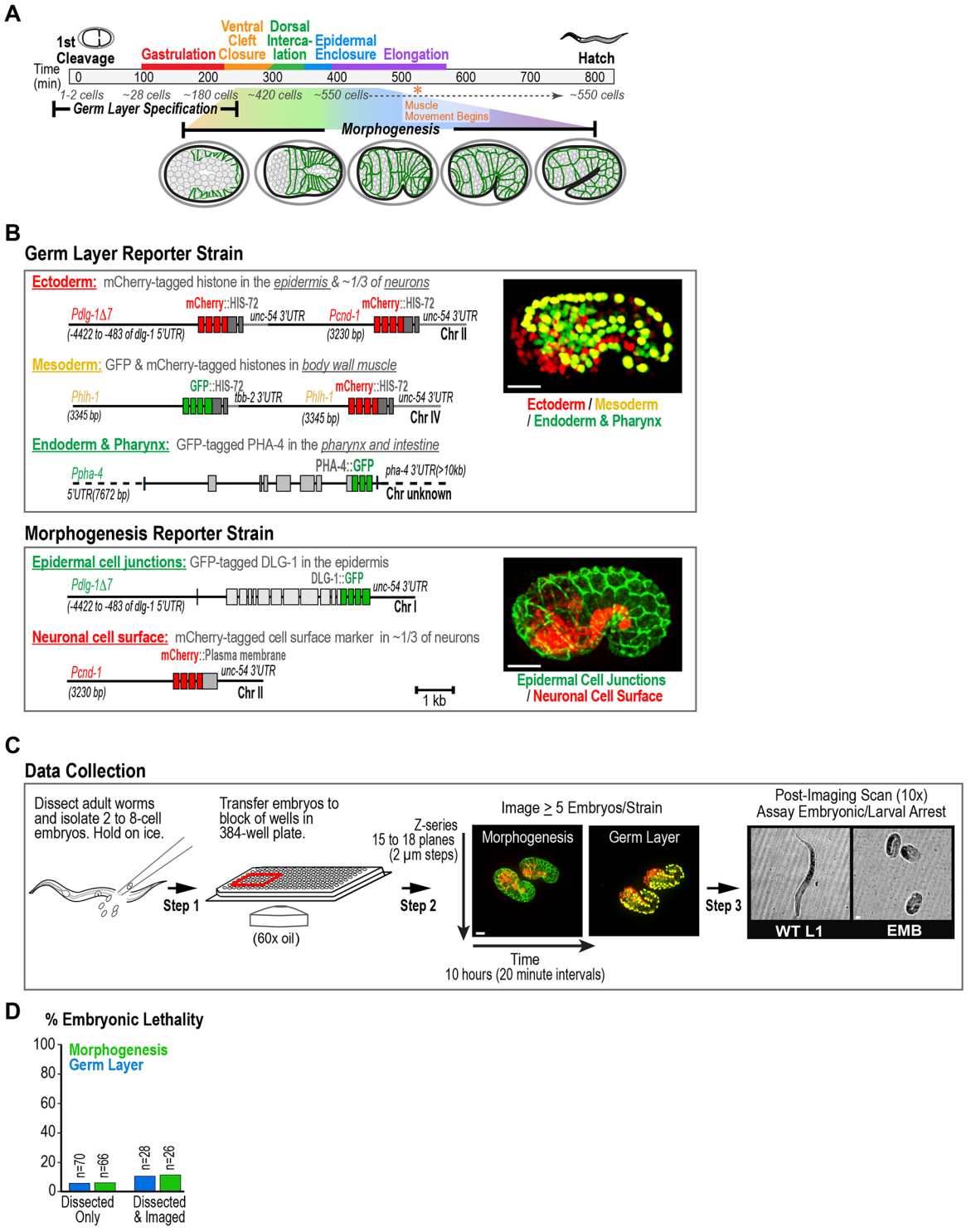

Fig. 1. Strains and a data collection method for high-content imaging of events during *C. elegans* embryogenesis. (A) Timeline of *C. elegans* embryonic development. Schematics illustrate morphogenetic events. (B) Schematics show transgenes in the Germ Layer (top) and Morphogenesis (bottom) strains. Images (right) show embryos from each strain during early elongation. (C) Schematics illustrate a data collection method that allows simultaneous monitoring of 80-100 embryos across multiple fields. (D) Graph plots embryonic lethality after the indicated manipulations. Scale bars: 10 µm.

RESULTS

Transgenic markers for high-content imaging of germ layer specification and morphogenesis during *C. elegans* embryogenesis

To monitor cell fate specification and morphogenesis during *C. elegans* embryogenesis, we developed a pair of strains that express different sets of fluorescent markers. The three germ layers – endoderm, ectoderm, and mesoderm – are a central organizing principle of embryonic development (Hall, 1999; Wolpert et al., 2015). An analysis of the *C. elegans* genes that are expressed in each germ layer indicated that the endoderm evolved first, followed by the ectoderm and mesoderm (Hashimshony et al., 2015), which

Development (2019) 146, dev174029. doi:10.1242/dev.174029

suggests that embryogenesis may employ germ layer-specific programs. To monitor effects on cell proliferation and positioning in the three germ layers, we constructed a Germ Layer reporter strain by using germ layer-specific promoters to express fluorescent nuclear markers. The ectoderm includes the epidermis and nervous system; to represent both components, we constructed a composite transgene on chromosome II that uses a modified *dlg-1* promoter (P*dlg-1Δ7*) (Sheffield et al., 2007) and the *cnd-1* promoter (Murray et al., 2008) to drive expression of an mCherry-tagged histone in the epidermis and ∼40% of the neurons in the embryo (Fig. 1B; Fig. S1). For neuronal expression, we also tested three other promoters; however, these were not optimal owing to non-specific (P*unc-33*, P*unc-119*) or lack of (P*rgef-1*) expression during embryogenesis. A GFP-tagged ectoderm transgene was also generated that was not used in the final strain (for a list of all transgenes generated, including ones not in the final strains, see Fig. S1, Table S1). The composite mesoderm transgene, constructed on chromosome IV, includes an mCherry- and GFP-tagged histone in tandem under control of the *hlh-1* promoter, which drives expression in body wall muscle (P*hlh-1*; Krause et al., 1994; Fig. 1B). Combining green and red reporters, rather than using a YFP tag, allows three color imaging by collecting *z*-stacks in two, rather than three, fluorescent channels, which increases the number of fields that can be imaged in a given time interval. To mark endoderm nuclei, we initially used the *elt-2* promoter to express mCherry- or GFP-tagged histone in the intestine. However, for the final strain we instead chose a transgene that expresses a GFP fusion with the PHA-4 transcription factor (Fig. 1B; Fakhouri et al., 2010; Zhong et al., 2010), because it labels nuclei in the pharynx as well as the intestine. The pharynx is a complex organ of mixed lineage that is part of the digestive tract (Altun and Hall, 2009; Mango, 2007). In summary, we generated a toolkit of strains with transgenes that express fluorescently tagged nuclear markers in the three germ layers (Fig. 1B, Fig. S1, Table S1), and combined three of these, which mark the ectoderm, mesoderm and endoderm/pharynx in red, yellow and green, respectively, in a composite Germ Layer reporter strain (Fig. 1B). To capture morphogenetic movements and cell shape changes during the second half of embryogenesis, we also generated a Morphogenesis reporter strain that uses the P*dlg-1Δ7* and P*cnd-1* promoters to express the epithelial junction marker DLG-1::GFP in the epidermis and an mCherry-tagged plasma membrane marker in a subset of neurons (Fig. 1B, Fig. S1, Table S1).

A high-content imaging method to capture germ layer specification and morphogenetic events during *C. elegans* embryogenesis

C. elegans embryogenesis takes ∼13 h, making it difficult to image enough embryos using one-at-a-time filming methods. To solve this problem, we developed a protocol using a spinning disk confocal microscope with point visiting capacity and a holder for 384-well glass-bottom plates (Yokogawa CV1000; Fig. 1C). For each condition, two- to eight-cell-stage embryos manually dissected from ∼10-15 hermaphrodites are loaded into one well with a mouth pipette. Although only 14 or fewer of the 384 wells are used in each experiment, the advantage of the 384-well plate is that it confines embryos to a small area, which enables rapid identification of multiple fields containing several embryos each. To ensure that embryos develop in a roughly synchronized fashion, the dissection media and imaging plate are kept on ice to stall embryogenesis until all wells have been loaded. We limit time on ice to 1 h, which is enough time for one person to dissect worms for around seven to eight conditions; up to 14 conditions can be imaged by having two people dissect in tandem.

The fluorescent reporters in our strains are first expressed ∼2.5 h after first cleavage. Thus, there is enough time to perform a low-resolution (10×) scan and select fields for high-resolution imaging before the markers are expressed. The close proximity of the wells allows high-resolution imaging with a 60×, 1.4NA oil lens. We typically collect green, red and brightfield *z*-series (15 to 18 *z*-planes at 2 µm intervals) of each field every 20 min for 10 h in a temperature-controlled room that allows us to maintain embryos at 21-23°C. This procedure allows imaging of 80-100 total embryos from up to 14 conditions in a single overnight run. Following imaging, we perform a low-resolution (10×) well scan to assess embryonic lethality and larval abnormalities. Although embryos subjected to dissection and imaging exhibited higher levels of embryonic lethality (∼11-12%) than embryos subjected to dissection alone (6%), lethality was still low Fig. 1D), suggesting that the procedure is well tolerated.

Visualization of developmental events in the Germ Layer and Morphogenesis strains

In this section, we highlight developmental events as they appear in embryos from the Germ Layer and Morphogenesis strains imaged using the above protocol (Movies 1 and 2). The comma stage (t=0, corresponding to ∼395 min post fertilization) is used as a temporal landmark to compare events in the two strains.

Morphogenesis strain

mCherry-marked neurons appear in two patches positioned on the left and right sides of the embryo anterior ∼120 min before the comma stage (Fig. 2A, top row, −120 and −100 min panels). Slightly later, two additional patches appear on the left and right sides in the embryo mid-region, so that the neurons appear to be partitioned into four quadrants (Fig. 2A,B; −60 min panels). During the 60 min before the comma stage, the neuron patches on the two sides of the embryo move towards each other until they meet at the midline (Fig. 2A,B; −60 to 0 min panels). The overlying epidermis, marked with the GFP-tagged apical junction marker, moves with the neurons, and seals at the midline to encase the embryo in skin (Ventral Enclosure, Fig. 2A-D). On the dorsal side of the embryo, the intercalation and subsequent fusion of the epidermal cells occurs during the same time interval (Dorsal Intercalation, Fig. 2E, Fig. S2A; Chisholm and Hardin, 2005). During the 80 min that follow the comma stage, the epidermis in the head is organized in concentric rings that appear to constrict and extend towards the anterior to encase the head in skin (Anterior Enclosure, Fig. 2F). During anterior enclosure, the bi-lobed neuronal structure that is formed when the anterior patches meet at the midline extends towards the anterior and is structured to form the early head ganglia and nerve ring (Fig. 2A,B,F; Hallam et al., 2000; Shah et al., 2017; Sulston et al., 1983). Between 60 and 120 min after the comma stage, the neurons below the midline intercalate via convergent extension to generate the ventral nerve cord (Ventral Nerve Cord Elongation, Fig. 2A,G; Shah et al., 2017).

Germ Layer strain

The ectoderm, mesoderm and endoderm/pharynx nuclear markers are expressed from ∼120 min before the comma stage (Fig. 2A, Fig. S2A). As the yellow mesoderm is a superposition of red and green signals, comparing images of the Germ Layer strain with images of strains expressing the three transgenes individually (Fig. S2B) can be helpful to understand the composite strain. PHA-4::GFP is in nuclei in the pharynx and endoderm, which are

Development (2019) 146, dev174029. doi:10.1242/dev.174029

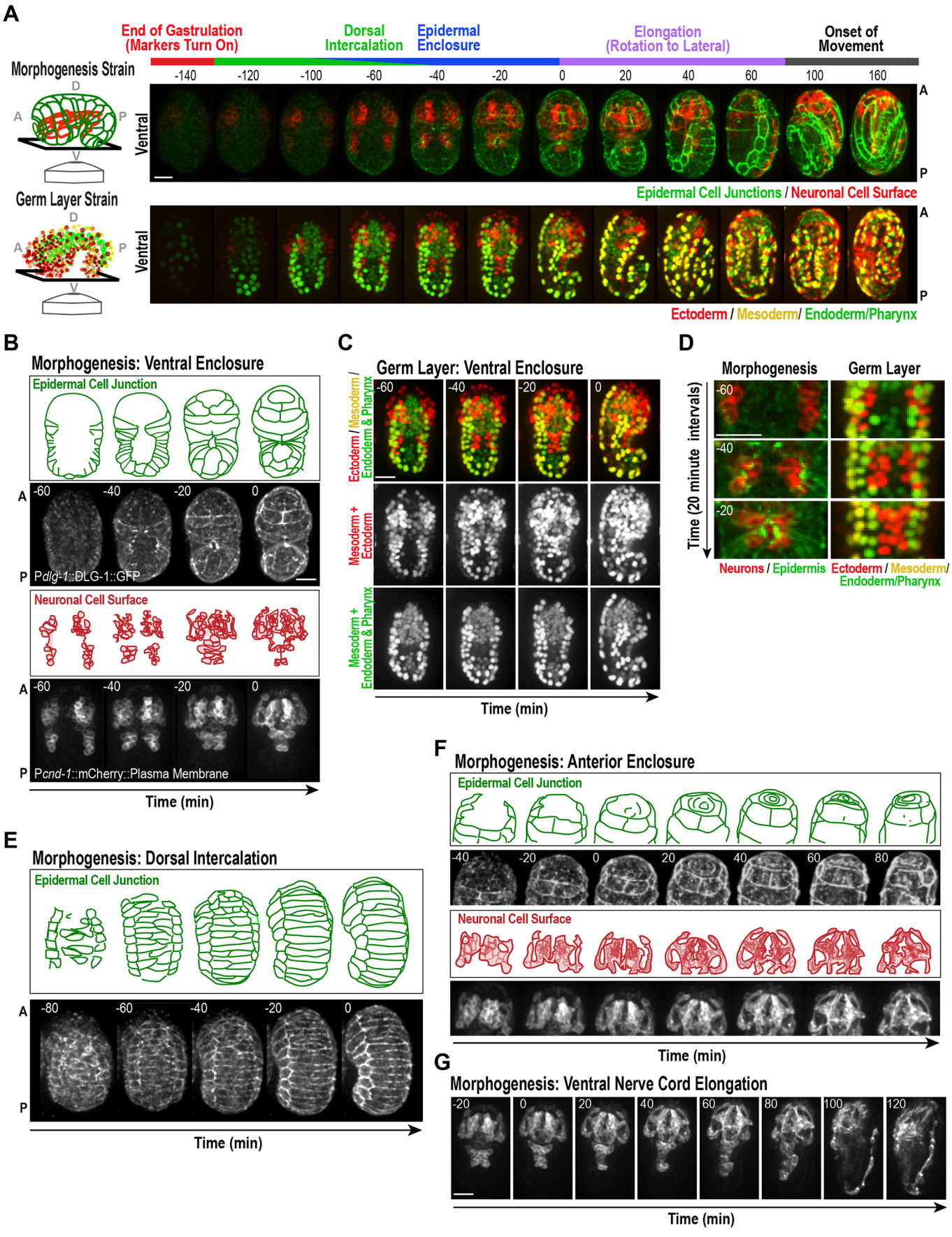

Fig. 2. See next page for legend.

Development (2019) 146, dev174029. doi:10.1242/dev.174029

Fig. 2. Visualization of key events during embryonic development in the Germ Layer and Morphogenesis strains. (A) Maximum intensity projections show a ventral view (illustrated in schematics) of embryonic development in the Morphogenesis (top) and Germ Layer (bottom) strains. Times are minutes relative to the comma stage (t=0). For a dorsal view see Fig. S2A. (B-G) Panels illustrate events during embryonic development in the Morphogenesis and Germ Layer strains. Images are maximum intensity projections and times are minutes relative to the comma stage (t=0). (B) Schematics and grayscale images illustrating the dynamics of epidermal cell junctions (top) and marked neurons (bottom) during ventral enclosure (ventral view) in the Morphogenesis strain. (C) Color and grayscale images showing movement of the ectoderm (red), endoderm/pharynx (green) and mesoderm (yellow, signal in both red and green channels) during ventral enclosure in the Germ Layer strain. (D) High magnification view of ventral enclosure in the Germ Layer and Morphogenesis strains. (E) Schematics (top) and grayscale images (bottom) illustrating epidermal cell junction dynamics during dorsal intercalation (dorsal view) in the Morphogenesis strain. (F) Schematics and grayscale images illustrating epidermal layer dynamics during head enclosure (top panels) and the concurrent restructuring of the nervous system (bottom panels). (G) Grayscale images of marked neurons showing elongation of the ventral nerve cord (enclosure through 2-fold stage) in the Morphogenesis strain. A, anterior; D, dorsal; P, posterior; V, ventral. Scale bars: 10 µm.

positioned in the central core of the embryo throughout development (Fig. S2B). The mesoderm nuclei, which are visible in both the red and green channels, form a cup-like structure that surrounds the green endoderm/pharynx nuclei in the posterior three-quarters of the embryo (Fig. S2B). As the mCherry fluorophore takes longer to mature than GFP, the mesoderm nuclei start out more green and then become fully yellow as the mCherry signal intensifies (Fig. S2B). When the neurons in the four patches become visible in the red channel in the Morphogenesis strain, the nuclei in the same neurons become visible in the red channel in the Germ Layer strain (−60 min timepoint in Fig. 2A and Fig. S2B). The nuclei in the epidermis, which are enriched at the lateral edges of the embryo and form a cap that sits over its anterior end, also appear in the red channel in the Germ Layer strain (−60 min timepoint in Fig. S2B). We conclude that the positioning of the germ layers and morphogenetic events during embryogenesis are clearly visualized using our strains and filming method.

Penetrant phenotypes are observed after RNAi in sensitized variants of the Germ Layer and Morphogenesis strains

A comparison of injection, soaking and feeding as delivery methods for double-stranded RNA (dsRNA) targeting a small set of test genes revealed that injecting L4 hermaphrodites with dsRNA and incubating them at 20°C for 24 h before dissection yielded the most reproducible results (data not shown). Next, we determined whether using a previously described RNA interference (RNAi)-sensitized background [*nre-1(hd20) lin-15b(hd126)*; Schmitz et al., 2007] would enhance the penetrance and severity of developmental phenotypes. We targeted 40 genes that are involved in a spectrum of developmental processes (Fig. 4B, Table S2.7) in four strains: the Germ Layer strain (Germ Layer control), the Germ Layer strain with RNAi-sensitizing mutations (Germ Layer sensitized), the Morphogenesis strain (Morphogenesis control), and the Morphogenesis strain with RNAi-sensitizing mutations (Morphogenesis sensitized). Time-lapse sequences of embryos (60×) and post scans (10×) were acquired (Fig. 3A).

In the absence of RNAi, addition of the sensitizing mutations to the Germ Layer and Morphogenesis strains did not alter hatching rates (Fig. 3B), indicating that the sensitizing mutations did not cause embryonic lethality on their own. However, for both strains, embryonic lethality was significantly higher following RNAi targeting the 40 test genes in the strains carrying the RNAi-sensitizing mutations compared with the control background (points above the diagonal in Fig. 3C; for a breakdown of which genes were enhanced see Fig. S3 and Table S2.1). To assess phenotypic severity, we scored the predominant arrest point for each depletion in each strain (Fig. 3A, from most to least severe: early arrest, comma arrest, 1.5-fold arrest, 2-fold arrest, 3-fold arrest, other embryonic lethal, larval abnormal/lethal). In both strains, arrest points were shifted from less to more severe in the sensitized background compared with the control (Fig. 3E,F; note that arrest point phenotypes for the same RNA tended to be slightly more severe in the Germ Layer strain compared with the Morphogenesis strain). As an example of a typical shift in severity between the control and sensitized backgrounds, RNAi of *dsh-2*, one of three *C. elegans* Disheveled homologs that contributes to WNT signaling, led to a late elongation arrest (2- to 3-fold) in the control background and 1.25-fold arrest with defects in neuronal organization and head morphology in the sensitized background (Fig. 3D, Movie 3).

Manual annotation of developmental defects observed in the Germ Layer and Morphogenesis strains partitions development genes into four broad classes

To assess the utility of our strains for profiling developmental phenotypes, we scored the time-lapse sequences for more detailed features (Fig. 4A; for defect examples and descriptions see Fig. S4 and Table S2.2). In the Germ Layer strain, the nuclear pattern was visually assessed at the comma stage (or arrest point, if earlier than comma stage). Embryos with an aberrant nuclear pattern, which can result from defects in either cell fate specification or cell positioning, were scored as having a 'cell fate/positioning defect'; nuclear abnormalities were also scored (Fig. S4B,C). In the Morphogenesis strain, we scored defects in nervous system and epidermal morphology, including defects in the row of seam cells, intercalation of the epidermal cells on the dorsal side of the embryo and ability of the epidermis to enclose the ventral side or head of the embryo (Fig. S4D-F). Note that the penetrance of three defects (ventral rupture, dorsal intercalation and seam cell defects) may be an underestimate, because the ability to score them depends on embryo orientation (for the number of embryos in each orientation see Table S2.3). The defects that were scored in the RNAi-sensitized background are summarized in Fig. 4B (for all defects scored in the control and RNAi-sensitized backgrounds for both strains see Table S2.3). Overall, this assessment partitioned the 40 genes into four broad classes (Fig. 4B): (1) genes whose inhibition led to cell fate and/or positioning defects, usually accompanied by arrest at or prior to the comma stage (Cell Fate or Positioning); (2) genes whose inhibition led to arrest at the comma or 1.5-fold stage along with ventral or anterior rupture and other morphogenetic defects (Early Morphogenesis); (3) genes whose inhibition led to defects in elongating beyond the 2-fold stage without a detectable effect on nuclear specification or positioning (Elongation); and (4) genes whose inhibition led to an arrest at or after the 3-fold stage and/or to larval abnormalities (Late Morphogenesis/Larval Development). Inspection of published expression profiles for the genes in our broad classes (Levin et al., 2012; Table S2.5) revealed that genes in the groups required for cell fate specification and/or positioning (group 1) and early morphogenesis (group 2) showed expression signatures that were consistent with either maternal expression (initially high and then falling gradually during embryogenesis) or relatively constant expression (suggesting both maternal and ongoing zygotic expression). In contrast, expression of genes

Development (2019) 146, dev174029. doi:10.1242/dev.174029

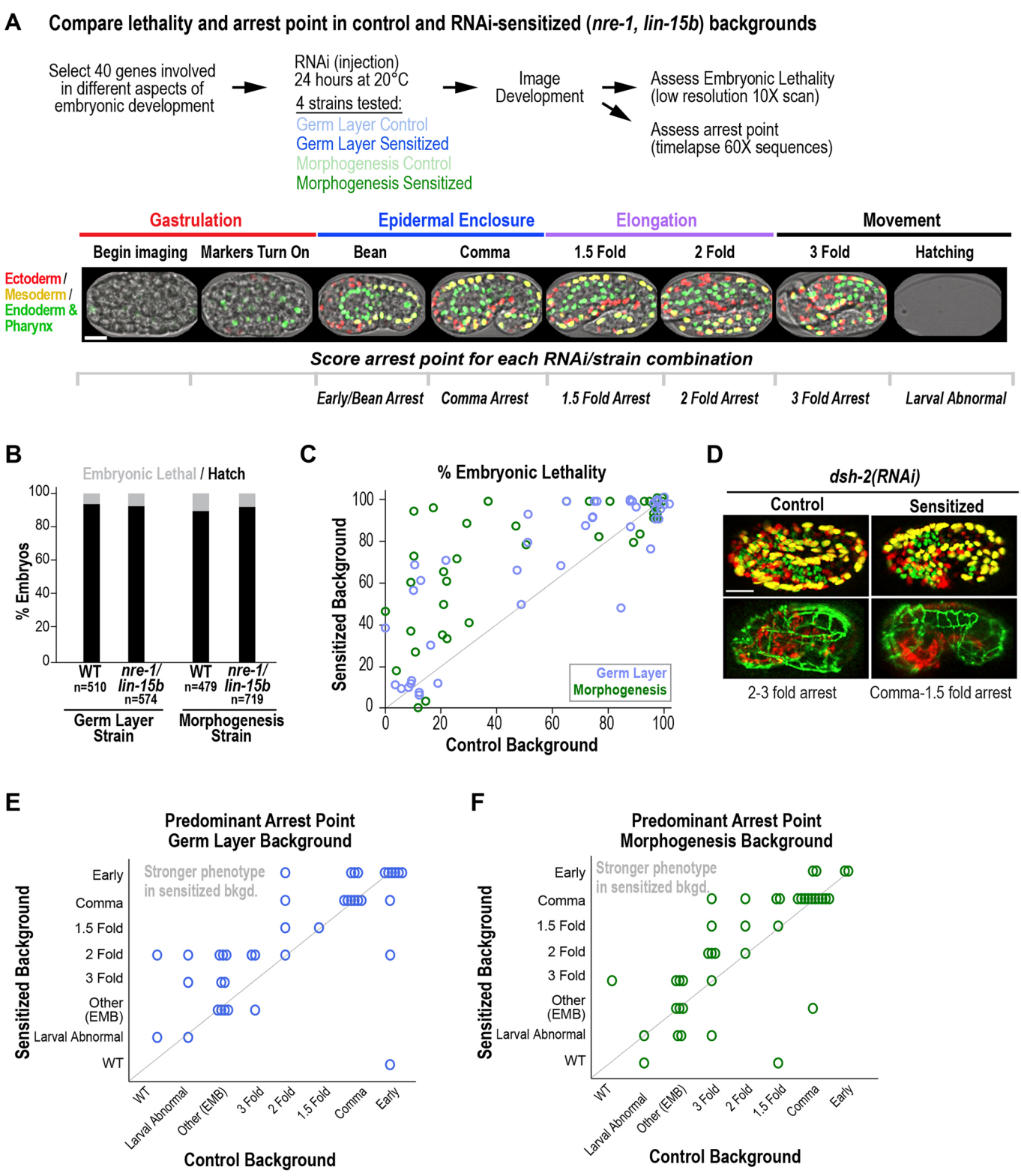

Fig. 3. See next page for legend.

required for elongation (group 3) or late morphogenesis/larval development (group 4) tended to be upregulated later during development, most commonly between the 7th AB-division and ventral enclosure, a time that has been proposed to correspond to a nematode phylotypic stage because of the number of crucial developmental genes that turn on (Levin et al., 2012).

Custom programs to crop and orient individual embryos for 4D data visualization and analysis

To isolate embryos for quantitative analysis, we developed custom software that crops out individual embryos from broader fields (Fig. 4C) and orients them based on asymmetry in the red channel signal (Fig. 4D), while also performing background subtraction and

Development (2019) 146, dev174029. doi:10.1242/dev.174029

Fig. 3. Penetrant phenotypes in RNAi-sensitized versions of the Germ Layer and Morphogenesis strains. (A) Outline of experiment to compare embryonic lethality and arrest points in the Germ Layer and Morphogenesis strains in the presence and absence of RNAi-sensitizing mutations for 40 developmental genes (top). Bottom images (central *z*-sections from the Germ Layer strain with bright-field images overlaid) illustrate major arrest points. (B) Stacked bar graph showing embryonic lethality (gray) and hatching (black) percentages for strains with and without RNAi-sensitizing mutations in the absence of RNAi. (C) Graph plots percentage embryonic lethality in the control (*x*-axis) versus the RNAi-sensitized background (*y*-axis) for each RNAi condition in the Germ Layer (blue) and Morphogenesis (green) strains. Points above the diagonal represent RNAi conditions with higher embryonic lethality in the sensitized background compared with the control. For a list of genes in each region see Fig. S3. (D) Representative images showing the terminal *dsh-2(RNAi)* phenotype in the Germ Layer (top) and Morphogenesis (bottom) strains without (left) and with (right) RNAi-sensitizing mutations. Marker colors for the two strains are as shown in Fig. 2A. (E,F) Graphs plot the predominant arrest point in the control (*x*-axis) versus the RNAi-sensitized background (*y*-axis) for each RNAi condition in the Germ Layer (E) and Morphogenesis (F) strains. Points above the diagonal represent RNAi conditions with an earlier arrest point in the sensitized background compared with the control. Scale bars: 10 µm.

correcting for signal attenuation with imaging depth. This program, which is accompanied by a graphical user interface (GUI), is compatible with image (tif) stacks acquired on most platforms and saves each embryo to a new, tightly cropped, anterior-posterior oriented stack (for details see Materials and Methods). We used the cropping program to generate tif files for individual embryos and assembled them into composite movies for each condition in each strain. The composite movies for each of our 40 RNAi conditions are available at datadryad.org/resource/doi:10.5061/dryad.kb79121 (Wang et al., 2019).

High-content imaging in the Germ Layer and Morphogenesis strains provides an efficient means to functionally profile genes required for cell fate specification and positioning

To evaluate the utility of the methodology described above for functional profiling, we began by analyzing the 18 genes in our test set that were scored with defects in cell fate specification or cell positioning and arrested before the 2-fold stage. These genes can be partitioned into three classes (Fig. 5A): (1) genes whose inhibition leads to incomplete cell fate specification because embryos arrest prior to the completion of cell division; (2) genes whose inhibition leads to normal numbers of each nuclei in each germ layer, despite an abnormal visual pattern, suggesting a role in cell positioning; and (3) bona fide genes required for cell fate specification. To partition the 18 genes between these classes, we segmented and counted the number of red, green and yellow nuclei in cropped Germ Layer image stacks at the comma stage (or arrest point, for embryos that arrested before the comma stage; Fig. 5B).

Genes whose inhibition results in incomplete cell fate specification, show low nuclear counts for all three germ layers. The strongest example in our test set was PLRG-1, a component of the CDC5L complex that is required for pre-mRNA splicing (Ajuh et al., 2000, 2001); *plrg-1* knockdown embryos exhibited an early arrest before marker expression in both strains (Fig. 5A-C; Movie 4). The *plrg-1(RNAi)* phenotype resembled that previously reported to result from blocking zygotic transcription (Nance and Priess, 2002; Powell-Coffman et al., 1996). Consistent with this idea, inhibition of a key RNA polymerase II subunit in our strains resulted in a similar early stage arrest before marker expression [*rpb-3(RNAi)*, data not shown]. Embryos in which *aps-1* was knocked down exhibited weaker incomplete specification, arresting with ∼25 fewer nuclei of each type than controls (Fig. 5B), along with severe epidermal and nervous system morphology defects (Movie 4). There were five class 2 genes that, despite exhibiting an abnormal nuclear pattern, had normal (*arx-1*, *arx-3*, *let-19*, *gex-2*) or only slightly reduced (*die-1*) nuclear counts for the three germ layers, suggesting a primary defect in cell positioning and/or early morphogenesis. Three of these genes encode regulators of actin assembly: ARX-1 and ARX-3 are components of the Apr2/3 complex (Pollard, 2017; Sawa et al., 2003), and GEX-2 is a component of the WAVE complex, which regulates the Arp2/3 complex in response to Rac signaling (Patel et al., 2008; Soto et al., 2002; Sullivan-Brown et al., 2016). Consistent with previous work, knockdown of all three genes led to a ventral rupture phenotype, particularly well captured in the Morphogenesis strain, in which the epidermis compressed into a patch on the dorsal side of the embryo (Fig. 5C; Movie 4), concurrent with an inside-out inversion that ejected the embryo contents out of its ventral side. Knockdown of the two other class 2 genes, *die-1* and *let-19*, gave distinct morphogenesis defects. DIE-1 is a C2H2 zinc-finger transcription factor that is implicated in cell intercalation (Heid et al., 2001; Rasmussen et al., 2013). In *die-1* knockdown embryos, the neuron patches on the right and left sides of the embryo came together as in controls, but dramatic defects in epidermal morphology, particularly on the dorsal and ventral sides of the embryo, prevented elongation and further development (Fig. 5C; Movie 4). In *let-19* knockdown embryos, defects in epidermal morphology were accompanied by anterior rupture (see Movie 4 and legend).

Eleven cell fate/positioning genes exhibited altered nuclear counts that suggested a primary defect in cell fate specification (Fig. 5B). These included four genes that are required for WNT signaling (*pop-1*, *mom-2*, *wrm-1* and *lit-1*), which controls asymmetric divisions in which the two daughter cells adopt distinct fates. POP-1 is a TCF/LEF family protein that is an essential component of a transcriptional repressor that prevents the expression of genes that specify endoderm fate; thus, *pop-1* inhibited embryos have extra endoderm (Jackson and Eisenmann, 2012; Sawa and Korswagen, 2013). *C. elegans* has several WNT proteins, but the most important of these in the embryo is MOM-2. Binding of the MOM-2 ligand to its receptor converts POP-1 from a transcriptional repressor to an activator that promotes endoderm fate. The divergent β-catenin WRM-1 and the Nemo-like kinase LIT-1 promote POP-1 nuclear export, which is essential for transduction of the WNT signal; thus, *mom-2*, *wrm-1* and *lit-1* knockdown embryos all lack endoderm and are expected to exhibit similar phenotypes (Jackson and Eisenmann, 2012; Sawa and Korswagen, 2013). Consistent with this expectation, RNAi of all three genes led to embryos that arrested with a similar sectored appearance (Fig. 5D, Movie 5, Fig. S5A). The similarity was particularly striking for *lit-1* and *wrm-1(RNAi)* embryos, in which a large patch of green nuclei ran along the length of the embryo on one side opposite a patch of red nuclei on the other side, with a cap of yellow nuclei at one end (Fig. S5A, regions marked with dotted outlines); both also exhibited similar disorganized epidermal and neuronal marker expression in the Morphogenesis strain (Fig. 5D, Movie 5). As expected, the *pop-1* phenotype was distinct from the phenotypes of the other three genes (Jackson and Eisenmann, 2012). In *pop-1* inhibited embryos, a stripe of green nuclei (presumably endoderm) appeared in the central core of the embryo. As development proceeded, patches of green nuclei appeared to be encased by an outer layer of red nuclei in one half of the embryo and an outer layer of yellow nuclei in the other half (Fig. S5A, regions marked with dotted outlines). Although the phenotypes were clearly distinct, the effects of the two classes of

Development (2019) 146, dev174029. doi:10.1242/dev.174029

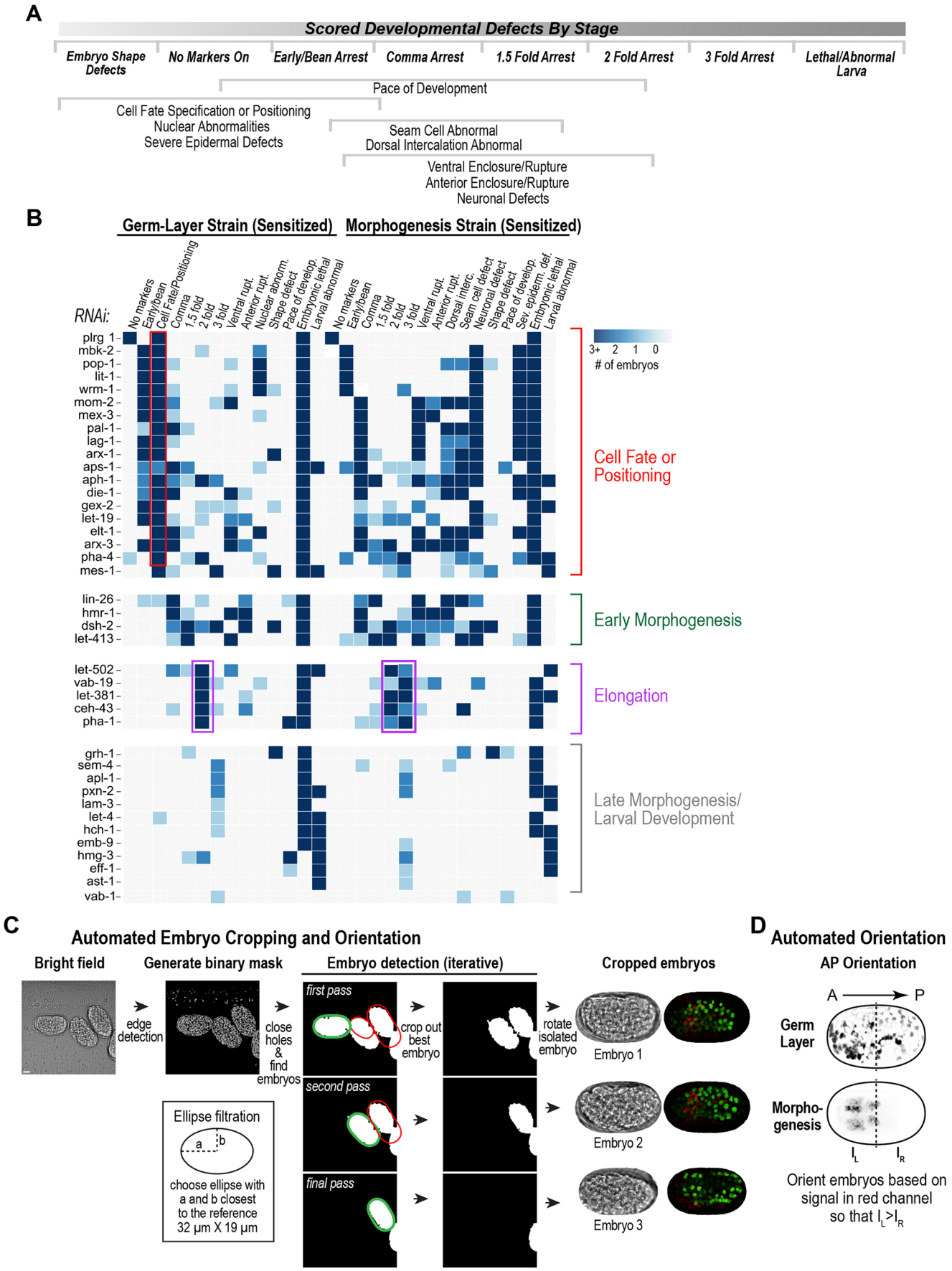

Fig. 4. See next page for legend.

Development (2019) 146, dev174029. doi:10.1242/dev.174029

Fig. 4. Manual annotation of defects in the Germ Layer and Morphogenesis strains partitions development genes into four broad classes. (A) Timeline illustrates arrest points and defects scored during the indicated time windows (brackets; see also Fig. S4 and Table S2.2). (B) Heatmap summarizing defects scored in the RNAi-sensitized Germ Layer and Morphogenesis strains. Color range indicates the number of embryos in which the defect was observed: lightest blue, 1 embryo; darkest blue, 3+ embryos. Dark blue coloring in the 'Embryonic lethal' and 'Larval abnormal' columns indicates >20% incidence in a 10× whole-well scan. (C) Graphic summary of automated embryo cropping procedure. (D) Schematic illustrating method for orienting embryos along the anterior-posterior axis. Scale bar: 10 µm.

WNT perturbation on nuclear counts (Fig. 5B) were similar owing to the fact that the green PHA-4 marker is expressed in both pharyngeal and endoderm nuclei, which masks the conversions between endoderm and pharyngeal fates that are characteristic of WNT signaling defects in a counting assay. In addition to genes that control WNT signaling, the cell fate specification genes also included two genes (*aph-1* and *lag-1*) that encode components of the Notch pathway. The Notch pathway mediates the cell-cell contact-based signaling required for anterior pharynx specification. APH-1 is a component of gamma secretase that cleaves the Notch receptor upon ligand binding to generate a fragment that translocates into the nucleus, where it interacts with LAG-1 to promote target gene transcription (Greenwald and Kovall, 2013). In the Germ Layer strain, *aph-1* and *lag-1* knockdown embryos exhibited an 'empty head' phenotype in which green pharyngeal nuclei were absent in the head region (Fig. 5B,D,F; Movie 5); the epidermis and neurons also exhibited similar abnormal dynamics in the Morphogenesis strain (Fig. 5D). Thus, high-content filming in the two reporter strains yielded distinct, reproducible signature phenotypes following inhibition of components of the WNT and Notch pathways.

Four of the bona fide cell fate specification genes were tissue-specific fate regulators. Inhibition of *pha-4*, a transcription factor that specifies the pharynx (Mango, 2007), resulted in a strong reduction in the number of green endoderm/pharynx nuclei (Fig. 5B) and an empty head phenotype similar to that seen with the loss of Notch pathway components; green endoderm nuclei were also absent (Fig. 5E,F). This was expected, as our green endoderm/pharynx reporter is PHA-4::GFP and confirms that our RNAi conditions target PHA-4 efficiently. The embryos also displayed defects in epidermal and neuronal organization and elongation consistent with loss of the pharynx (*pha-4* sequences at datadryad.org/resource/doi:10.5061/dryad.kb79121; Wang et al., 2019). Knockdown of *elt-1*, which encodes a transcription factor that is required for epidermal specification (Gilleard and McGhee, 2001; Page et al., 1997), led to a marked reduction in red ectoderm nuclei in the Germ Layer strain (Fig. 5B) and a striking lack of an outer epidermal layer in the Morphogenesis strain (Fig. S4E,F). Two cell fate specification genes were involved in mesoderm specification, *pal-1* and *mex-3*. PAL-1 is a conserved homeodomain protein that specifies the C and D blastomeres, which produce primarily body wall muscle (Hunter and Kenyon, 1996). Knockdown of *pal-1* in the Germ Layer strain led to a reduction in the number of mesoderm nuclei (Fig. 5B) and arrest with a visible void in the posterior where the mesoderm normally resides (Fig. 5E,F). MEX-3 binds the 3′ UTR of the *pal-1* message and represses its expression in the embryo anterior (Hunter and Kenyon, 1996; Pagano et al., 2009). Thus, *mex-3* inhibition leads to ectopic PAL-1 expression and an anterior-to-posterior cell fate transformation that produces extra muscle (Draper et al., 1996). Consistent with this, *mex-3* knockdown in the Germ Layer strain led to a dramatic increase in number of yellow muscle nuclei at the expense of red and green nuclei (Fig. 5B,E). In summary, distinct reproducible phenotypes, consistent with their established roles, were observed for each of the four established tissue-specific regulators in our test gene set.

A gene for which our analysis provided new insight is *mbk-2*, which encodes a dual-specificity YAK-1-related (DYRK) family kinase that controls the maternal-to-zygotic transition. Penetrant MBK-2 depletion leads to a complex phenotype that includes cell division defects owing to failure to degrade the microtubule-severing complex katanin at the meiosis-to-mitosis transition (Robertson and Lin, 2015). Under our conditions in the Germ Layer strain with the RNAi-sensitizing mutations, *mbk-2(RNAi)* led to a bimodal phenotype: half of the embryos exhibited an early arrest with relatively few nuclei, consistent with cell division defects; however, the other half, presumably those in which *mbk-2* was only partially inhibited, exhibited a muscle in excess (Mex) phenotype, similar to *mex-3* inhibition (Fig. 5B,E; Movie 6). Consistent with the idea that the Mex phenotype results from partial inhibition of *mbk-2*, six out of six embryos exhibited the Mex phenotype in the control background (Fig. S5B, Table S2.3). MEX-3 lies downstream of MEX-5/6, two partially redundant zinc-finger proteins that prevent MEX-3 degradation in the embryo anterior (Hunter and Kenyon, 1996; Schubert et al., 2000); as expected, *mex-5/6* knockdown resulted in a phenotype that was essentially identical to *mex-3* knockdown (Movie 6). Previous biochemical work suggested that MBK-2 activates MEX-5/6 by phosphorylation at a specific site that enables docking of a second kinase, PLK-1 (Fig. 5G; Nishi et al., 2008). Despite the elegant *in vitro* biochemistry, direct *in vivo* evidence for MBK-2 function in cell fate specification has been lacking (Robertson and Lin, 2015). Our observation that *mbk-2* inhibited embryos can exhibit a classic Mex phenotype fills this gap, providing *in vivo* support for proposed role of MBK-2 in preventing PAL-1 expression in the embryo anterior (Fig. 5G). These results suggest that high-content analysis in our strains has the potential to provide new insights for other well-characterized development genes.

Filming in the Germ Layer and Morphogenesis strains enables functional classification of genes required for elongation

After epidermal enclosure, the embryo elongates 4-fold in length, accompanied by a 2-fold decrease in diameter, to achieve its final shape (Vuong-Brender et al., 2016; Fig. 6A). Five genes in our test set encoded proteins that first become essential at this stage (Figs 4B and 6B). Elongation can be divided into two phases that begin before and after the onset of muscle contraction (Vuong-Brender et al., 2016; Fig. 6A). During the first phase, elongation is driven by changes in epidermal cell shape that require stimulation of the small GTPase RhoA (RHO-1 in *C. elegans*), leading to increased actomyosin contractility in seam cells (green in Fig. 6A), concurrent with suppression of the same pathway in the dorsal and ventral epidermis (red in Fig. 6A; Vuong-Brender et al., 2016). RhoA promotes actomyosin contractility by activating the LET-502/Rho kinase, which controls the activity of myosin II (Gally et al., 2009; Wissmann et al., 1997). The second phase begins when the muscles start to contract (Vuong-Brender et al., 2016). Muscles, which are internal to the epidermis, are attached to the cuticle outside the epidermis via transepithelial attachment structures that consist of intermediate filaments anchored to fibrous organelles that span the plasma membrane on the apical and basal sides of the epithelium (Fig. 6A; Zhang and Labouesse, 2010). Two of the five genes that

Development (2019) 146, dev174029. doi:10.1242/dev.174029

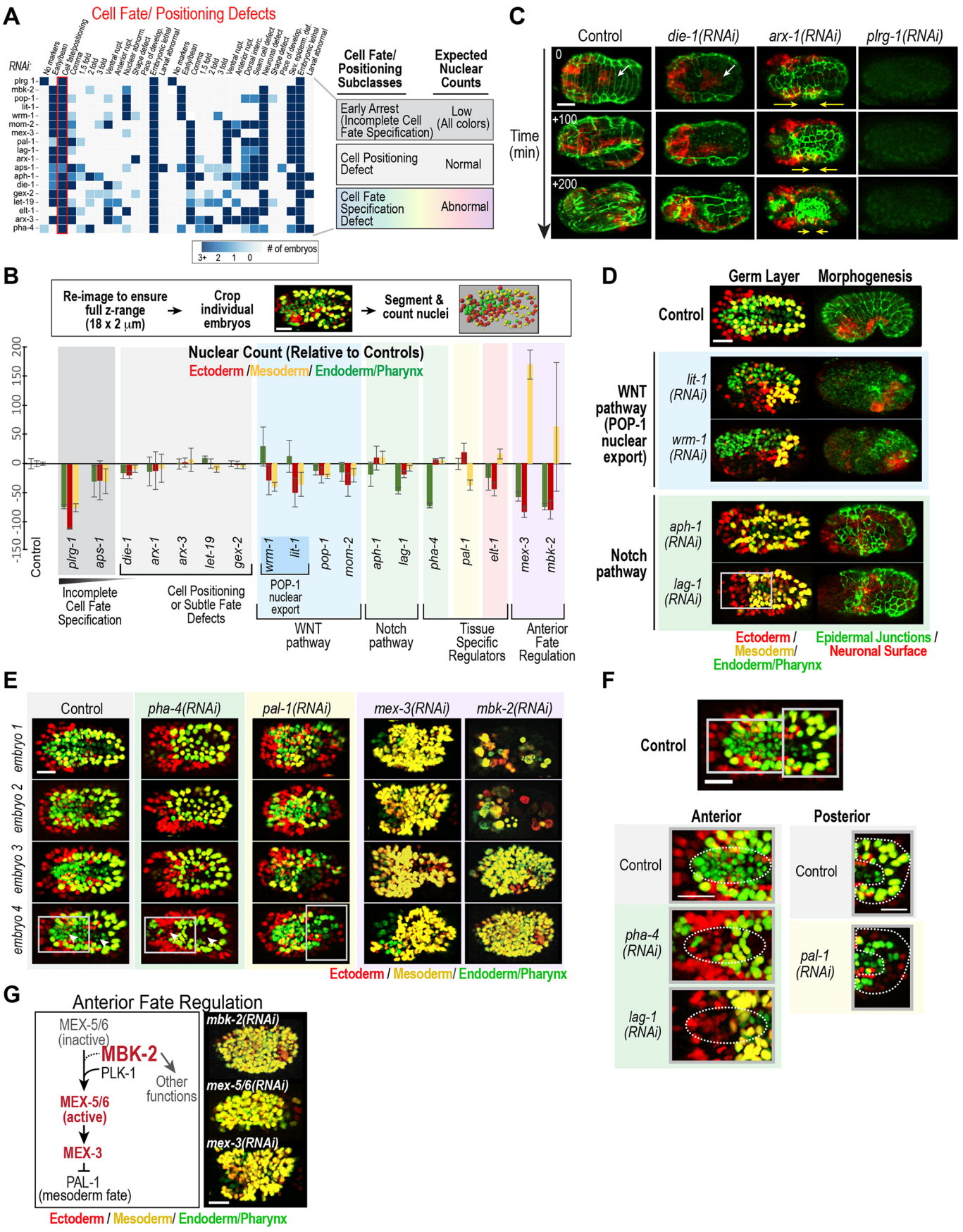

Fig. 5. See next page for legend.

Development (2019) 146, dev174029. doi:10.1242/dev.174029

Fig. 5. Imaging in the Germ Layer and Morphogenesis strains is an efficient means to functionally profile genes that are required for cell fate specification and/or cell positioning. (A) Genes required for cell fate and/or positioning (heatmap region reproduced from Fig. 4B) are partitioned into three subclasses based on nuclear counts. (B) Schematic outlines nuclear counting procedure (top). Graph (bottom) plots number of nuclei in each germ layer for each condition after subtraction of the mean value for controls (mean number of embryos per condition=6; *n*=9 for controls). Error bars represent s.d. (C) Representative time-lapse images showing a dorsal view in the RNAi-sensitized Morphogenesis strain for a control, one class 1 (*plrg-1*) and two class 2 (*arx-1*, *die-1*) genes. White arrows in the control and *die-1(RNAi)* images point to cell-cell boundaries on the dorsal side of the control embryo that are absent in *die-1(RNAi)* embryos. Yellow arrows track compression of the dorsal epidermis coincident with ventral rupture in the *arx-1(RNAi)* embryo. (D) Representative images show arrest point phenotypes in the Germ Layer strain following knockdown of two components of the WNT signaling pathway (*lit-1* and *wrm-1*) and two components of the Notch pathway (*lag-1* and *aph-1*) compared with a similarly staged control embryo (top). The gray box marks a region shown at higher magnification in F. (E) Four embryos are shown for each condition to illustrate embryo-to-embryo variation in phenotype. The top control panel (embryo 1) is reproduced for comparison from Fig. 5D. All phenotypes were highly consistent, with the exception of *mbk-2(RNAi)* which was bimodal, exhibiting either an early (top) or later (bottom) arrest. Arrowheads mark green PHA-4::GFP-labeled pharynx and endoderm nuclei that are missing in *pha-4(RNAi)* embryos. Gray boxes mark regions shown at higher magnification in F. (F) Top shows the bottom control embryo from E with its anterior and posterior regions marked (gray boxes). Bottom left shows a higher magnification view of the anterior regions of selected control, *pha-4(RNAi)* and *lag-1(RNAi)* embryos. White dotted ovals mark the region where the PHA-4::GFP-expressing pharynx nuclei in control embryos are missing in *pha-4* and *lag-1(RNAi)* embryos. Bottom right shows a higher magnification view of the posterior regions of a control and *pal-1(RNAi)* embryo. The region outlined with the white dotted line marks the cup of mesoderm nuclei in the posterior of the control embryo that is absent in the *pal-1(RNAi)* embryo. (G) Schematic (left) shows a simplified version of the pathway by which MEX-5/6 activates MEX-3, which inhibits PAL-1 to suppress mesoderm fate in the embryo anterior (Kuersten and Goodwin, 2003). Images (right) illustrate the similar Germ Layer strain phenotypes for *mbk-2(RNAi)*, *mex-5/6(RNAi)* and *mex-3(RNAi)*. The *mbk-2(RNAi)* and *mex-3(RNAi)* images are reproduced from panel E for comparison. Scale bars: 10 µm.

are required for elongation are *let-502*, which is required for actomyosin contractility during phase 1 (Gally et al., 2009; Wissmann et al., 1999), and *vab-19*, which is essential for transepithelial muscle attachment during phase 2 (Ding et al., 2003; Fig. 6A,B). Although both inhibitions led to arrest at the 2- to 3-fold stage, their phenotypes were clearly distinct. Embryos in which *let-502* was knocked down arrested without further movement, whereas *vab-19* knockdown embryos continued to quiver and the epidermis exhibited a crumpled end-stage phenotype (Fig. 6C; Movie 7).

Three additional genes exhibited specific elongation defects (*ceh-43*, *pha-1* and *let-381*). We will discuss *ceh-43* and *let-381* here (for a discussion of *pha-1* see Fig. S6). CEH-43 is the sole *C. elegans* ortholog of the Distalless/Dlx homeobox genes that are involved in appendage development in animals (Aspöck and Bürglin, 2001; Panganiban and Rubenstein, 2002). Previous work has shown that CEH-43 is expressed in the epidermis, neurons and neuronal support cells in the head, and that cells leak out of the embryo from a hole in the epidermis at the tip of the head in *ceh-43* knockdown embryos (Aspöck and Bürglin, 2001). It was also reported that the pharynx disconnected from the buccal cavity (mouth) in these embryos and retracted into the embryo [or pharynx unattached (Pun) phenotype]. Following *ceh-43* knockdown in the Germ Layer strain, we observed pharyngeal cells leaking out through a hole in the head; however, all of the pharyngeal cells ended up outside the embryo and did not subsequently retract (blue arrows in Fig. 6C, Fig. S5C; Movie 7). As expulsion of the pharynx precludes its connection to the buccal cavity, it is not surprising that elongation, which likely requires the mechanical integrity of this connection, fails in *ceh-43* inhibited embryos.

FoxF forkhead transcription factors are generally implicated in mesoderm development (Amin et al., 2010; Mazet et al., 2006). Consistent with this, the single *C. elegans* FoxF-related transcription factor, LET-381, is required to specify the fate of the non-muscle mesoderm descendants of the M mesoblast (coelomocytes) during the larval stages (Amin et al., 2010). LET-381 is also expressed in a number of unidentified cells in the head during embryogenesis (Amin et al., 2010). Mutants in *let-381* are embryonic lethal, and hatched *let-381* larva have been reported to exhibit short or 'dumpy' phenotypes (Amin et al., 2010; Simmer et al., 2003); however, embryonic elongation arrest phenotypes have not previously been described. Our analysis indicates that *let-381* knockdown results in phenotypes in the Germ Layer and Morphogenesis strains that are essentially identical to the *vab-19* knockdown phenotypes (Fig. 6C). Like *vab-19*, and in contrast to the *ceh-43* and *pha-1* knockdowns, *let-381* knockdown did not lead to head-specific defects, which suggests that LET-381 may have a role in the assembly of transepithelial attachment structures. Further investigation will be needed to address this possibility.

Overall, the analysis of the 40-gene set indicates that high-content filming in the Germ Layer and Morphogenesis strains provides a rapid and effective means to generate precise phenotypic signatures for functional classification of genes that are involved in morphogenesis as well as in cell fate specification during embryonic development.

DISCUSSION

Here, we describe a high-content imaging approach that captures both early and late developmental events during *C. elegans* embryogenesis. We also present a data collection procedure that allows simultaneous monitoring of development in 80-100 embryos and a custom program that generates cropped, oriented image stacks of individual embryos to facilitate data analysis. We anticipate that the methodology described here will be broadly useful for the characterization of developmental phenotypes and will also provide a framework for large-scale screening approaches to systematically characterize genes required for embryonic development.

Lineage tracing-based methods to analyze development were pioneered by groups that were interested in understanding cell fate specification (Bao et al., 2006; Du et al., 2015, 2014; Giurumescu et al., 2012; Ho et al., 2015; Murray et al., 2008, 2012; Santella et al., 2010). One outcome of this work has been a description of the regulatory network that controls founder cell specification in the embryo (Du et al., 2015, 2014). However, although the power of lineage tracing-based approaches is clear, they also have limitations. In particular, lineage tracing is labor-intensive, requires expertise beyond that available in the majority of labs, is low throughput and is not sufficient for the analysis of morphogenetic events. A major goal of our work was to develop a technically straightforward approach that, by virtue of the combinatorial expression of carefully selected fluorescent markers, could be implemented in any lab to provide a first-pass analysis of a broad spectrum of key events during embryogenesis. To demonstrate the utility of the method, we used it to monitor development in cohorts of embryos after knocking down a test set of 40 genes that act in diverse developmental events. The results show that the method generates distinct, reproducible phenotypic signatures that provide functional insight and enable the classification of genes across a

Development (2019) 146, dev174029. doi:10.1242/dev.174029

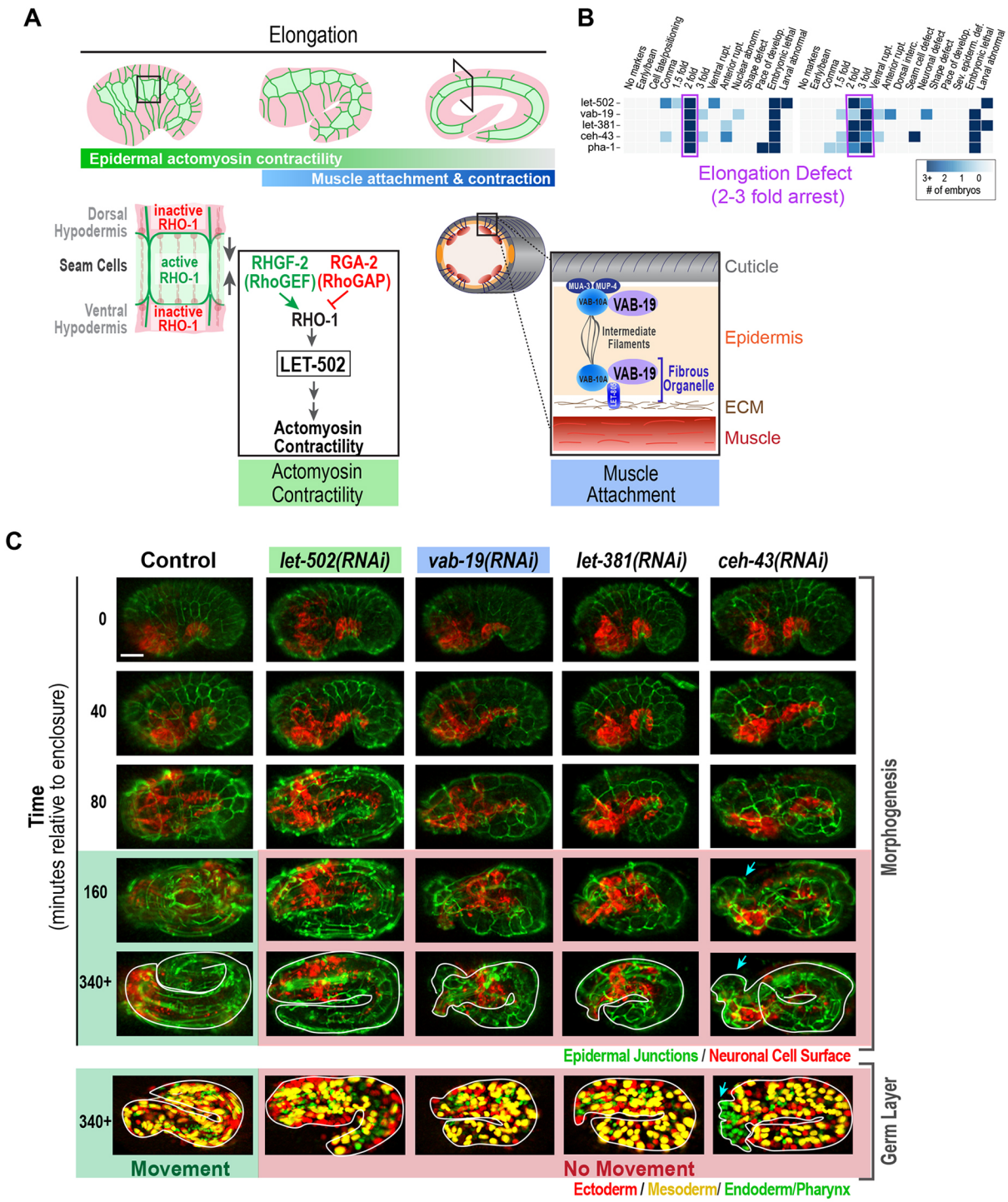

Fig. 6. High-content imaging in the Germ Layer and Morphogenesis strains enables functional classification of genes that are required for elongation. (A) Top schematics illustrate cell-shape changes in the seam (green) and dorsal/ventral (red) epidermal cells during elongation, and the two temporally overlapping processes that drive elongation (adapted from Vuong-Brender et al., 2016). Bottom schematics outline two key pathways that contribute to elongation. (B) Genes required for elongation (heatmap region reproduced from Fig. 4B). (C) Representative time-lapse images in the RNAi-sensitized Morphogenesis strain of a control embryo and knockdown embryos for four genes that are specifically required for elongation (top). Representative images showing arrest point phenotypes in the RNAi-sensitized Germ Layer strain compared with a control embryo at a comparable stage (bottom). For more complete time-lapse series see Fig. S5C. Elongating embryos were outlined to make embryo shape at arrest more visible. Inhibition of *ceh-43* leads to irregularities in the anterior region (blue arrows). Green shading indicates successful elongation and movement within the eggshell, whereas red shading indicates arrest and failure to move. Scale bar: 10 µm.

broad spectrum of processes that are required for cell fate specification and tissue morphogenesis. In addition to being consistent with previous work on individual genes, our test set data provided *in vivo* evidence for a role for MBK-2 in mesoderm fate specification, extending previous biochemical work (Nishi et al., 2008), and suggested a role for LET-381 in elongation.

Development (2019) 146, dev174029. doi:10.1242/dev.174029

In addition to providing a standardized means for the initial characterization of developmental phenotypes in the embryo, the method described here is well suited for the systematic analysis of cohorts of embryos following RNAi-mediated knockdown of each of the ∼2000 genes that are essential for embryonic development. An ongoing project is already generating a large dataset of 3D time-lapse sequences in the Germ Layer and Morphogenesis reporter strains following each gene knockdown. We expect that the *C. elegans* community will take advantage of the approach described here to characterize mutants, thereby providing additional data that will add to the RNAi-based dataset. An important future direction will be the development of automated methods to identify phenotypic features in time-lapse data and to compare and classify early and late developmental phenotypes. Although manual analysis methods are sufficient for the analysis of small datasets, automated methods will be essential to ensure consistent data analysis at reasonable throughput across larger datasets.

MATERIALS AND METHODS

Strain construction

All transgenes, except for the transgene that expresses PHA-4::GFP (Fakhouri et al., 2010; Zhong et al., 2010), were generated using a transposon-based strategy (mos1-mediated single copy insertion; Frøkjær-Jensen et al., 2008). Promoter sequences can be found in the Supplementary Material. In the Germ Layer strain, ectoderm nuclei were marked by expressing mCherry::HIS-72 using a truncated *dlg-1* promoter (-4422 to -483 of *dlg-1* 5′ UTR; epidermis) and a *cnd-1* promoter (3230 bp of *cnd-1* 5′ UTR; ∼40% embryonic neurons; Murray et al., 2008). The truncated *dlg-1* promoter deletes the seventh and most proximal GATA motif in the promoter region (P*dlg-1Δ7*; Pauli et al., 2006), and thus drives expression in the epidermis, but not in the pharynx or intestine at the embryonic stage (Pauli et al., 2006). A subset of the mesoderm nuclei (muscle cells) were marked yellow by the expression of both GFP::HIS-72 and mCherry::HIS-72 under control of the *hlh-1* promoter (3345 bp of *hlh-1* 5′ UTR). Nuclei in the endoderm (intestine) and pharynx (mixed lineage) were marked green by expressing a nuclear-localized transcription factor, PHA-4::GFP, under the control of endogenous *pha-4* regulatory elements (GFP inserted at the C terminus of the PHA-4 coding sequence by fosmid recombineering; Fakhouri et al., 2010; Zhong et al., 2010). The two transgene modules encoding the red ectoderm nuclei, P*dlg-1Δ7::mCherry::his-72* and P*cnd-1::mCherry::his-72*, were cloned in tandem into pCFJ151 (Addgene plasmid #19330) for insertion at *ttTi5605* on chromosome II. The two transgene modules encoding the yellow muscle nuclei, P*hlh-1::mCherry::his-72* and P*hlh-1::GFP::his-72*, were cloned in tandem into pCFJ178 (Addgene plasmid #19331) for insertion at *cxTi10882* on chromosome IV. Single-copy transgenes were generated by injecting a mixture of the above transgene constructs, a plasmid encoding the Mos1 transposase [pCFJ601, P*eft-3::Mos1 transposase* (Addgene plasmid #34874), 50 ng/µl] and three plasmids encoding fluorescent markers for negative selection [pCFJ90, P*myo-2::mCherry* (Addgene plasmid #19327), 2.5 ng/µl; pCFJ104, P*myo-3::mCherry* (Addgene plasmid #19328), 5 ng/µl; and pGH8, P*rab-3::mCherry* (Addgene plasmid #19359), 10 ng/µl] into strains EG6429 (outcrossed from EG4322; *ttTi5605*, chromosome II) or EG6250 (*cxTi10882*, chromosome IV). After one week, moving worms without fluorescent markers were identified as candidates and transgene integration was confirmed in their progeny using PCR that spanned both homology regions. After integration transgenes were outcrossed 6× into the wild-type N2 background. The transgene that expressed PHA-4::GFP (stIs10389) was isolated from RW10425 [obtained from the *Caenorhabditis* Genetics Center (CGC); Fakhouri et al., 2010; Zhong et al., 2010] by outcrossing 6× into N2 and selecting for the PHA-4::GFP transgene. The three transgenes were then combined together to obtain the final Germ Layer strain (OD1719). To make the strain more sensitive to RNAi, two linked mutations [*nre-1(hd20) lin-15b(hd126)*; Schmitz et al., 2007] were introduced to obtain the sensitized Germ Layer strain (OD1854).

A second set of transgenes was generated to visualize the apical junctions of epidermis and the cell surface of neurons. The epithelial junctions were marked in the epidermis by expressing DLG-1::GFP using the P*dlg-1Δ7* promoter; this transgene was cloned into pCFJ352 (Addgene plasmid #30539) for insertion at ttTi4348 on chromosome I. The cell surface of neurons was marked by expressing a mCherry-tagged plasma membrane marker (Audhya et al., 2005) using the *cnd-1* promoter (3230 bp of *cnd-1* 5′ UTR; ∼40% of embryonic neurons; Murray et al., 2008); this transgene was cloned into pCFJ151 for insertion at ttTi5605 on chromosome II. Single-copy transgenes were generated as described above and outcrossed 8× (P*dlg-1Δ7::dlg-1::GFP*) or 6× (P*cnd-1::mCherry::PH*) into the wild-type N2 background. The two transgenes were then crossed together to generate the Morphogenesis strain (OD1689). To make the strain more sensitive to RNAi, two linked mutations [*nre-1(hd20) lin-15b(hd126)*; Schmitz et al., 2007] were introduced to obtain the sensitized Morphogenesis strain (OD1853). To ensure the RNAi enhancer mutations were introduced, OD1853 was backcrossed 4× into the RNAi enhancer strain CZ8244 to obtain the final sensitized Morphogenesis strain (OD2416).

RNA interference

dsRNAs were generated using the primers in Table S2.7 to amplify a 500-1000 bp coding region of the corresponding gene from genomic DNA. PCR reactions were cleaned (QiaQuick, Qiagen) and used as templates for T3 and T7 transcription reactions (Megascript T3 and T7 kits, Ambion), which were combined, cleaned (RNeasy, Qiagen) and annealed by adding 3× Soaking buffer (32.7 mM Na_2HPO_4, 16.5 mM KH_2PO_4, 6.3 mM NaCl, 14.1 mM NH_4Cl) to a final concentration of 1× and incubating the reactions at 68°C for 10 min followed by 37°C for 30 min.

RNAi was performed by injecting dsRNA into 12-18 L4-stage worms each from the Morphogenesis and Germ Layer strains. Injected worms were allowed to recover on OP50 seeded plates for 20-22 h before dissection. Previous analysis of the expression of the genes in our test set (Table S2.5) suggests that genes that are required for cell fate specification and early morphogenesis generally exhibit either maternal or both maternal and zygotic expression, whereas genes whose inhibition results in later phenotypes, tend to be zygotically expressed. Thus, getting good developmental phenotypes requires inhibition of both maternal and zygotic gene expression. In our experience, the key variable is the time between injection and embryo filming, which determines both the extent of maternal protein depletion and the amount of injected dsRNA loaded into the embryo. After the dsRNA is injected, the maternal mRNA that corresponds to the gene is degraded. Depletion of the pre-existing protein then requires embryo production, which ejects the pre-existing maternal protein from the germline by loading it into the forming embryos. The shortest incubation time that allows consistent maternal depletion is ∼20 h at 20°C, and the depletion improves up to ∼36-42 h after injection. The prevention of zygotic gene expression in the embryos depends on the amount of injected dsRNA that is loaded into the embryo. The amount of RNA loaded is highest at ∼5-10 h after injection, when embryos that have incorporated injected material first begin to be fertilized, and then declines after this point. By 36-48 h after injection, we have often observed that zygotic inhibition starts to be lost, presumably because insufficient RNA is loaded into the embryos that are produced at these late timepoints after injection. Consequently, we chose 20-22 h after dsRNA injection as the optimum timepoint for both maternal protein depletion and inhibition of zygotic gene expression in the isolated embryos.

Embryo dissection and image acquisition

For each RNAi condition, ∼10 gravid adults were dissected in ice cold tetramisole hydrochloride (TMHC; 0.1 mg/ml) dissolved in M9 medium, and two- to 16-cell-stage embryos were transferred by mouth pipette to individual wells containing 70 µl of the same solution in a glass-bottom 384-well Sensoplate (Greiner Bio-One), which was maintained on ice until dissection was completed for all conditions. For each overnight run, 14 conditions were prepared: a control for each strain (two wells) and six RNAi conditions in both strain backgrounds (12 wells). Mouth pipettes were switched and dissection equipment cleaned between dissections of the worms for each condition to prevent cross-contamination. Before imaging,

Development (2019) 146, dev174029. doi:10.1242/dev.174029

the 384-well plate was spun for 1 min at 600 ***g*** to seat the embryos. Embryos were imaged using a CV1000 confocal scanner box equipped with a microlens-enhanced dual Nipkow spinning disk (Yokogawa Electric Corporation), a 512×512 EM-CCD camera (Hamamatsu), a high-precision auto-XY-Stage (designated resolution 0.1 µm) and motorized *z*-axis control (designated resolution 0.1 µm). The room was maintained at 16°C to allow the instrument to maintain the imaging chamber between 21 and 23°C. Fields with suitable embryos were identified by performing a pre-scan of each well using a 10×0.4 NA U-PlanApo objective. Two (controls) or four (RNAi conditions) fields, with between one and five embryos per field, were imaged. Overall, a total of four to 15 embryos from each strain for each condition were selected for high-resolution imaging. Each field was imaged by using a 60×1.35NA U-PlanApo objective to acquire 15 (initial screen) or 18 (nuclear counting) *z*-sections at 2 µm intervals every 20 min for 10 h. Imaging conditions were as follows: brightfield, 90% power, 25 ms, 20% gain; 488 nm, 100% power, 200 ms, 60% gain; 568 nm, 45% power, 150 ms, 60% gain. To assess embryonic lethality, wells were post-scanned 24 h after the start of imaging using bright-field optics and a 10×0.4 NA U-PlanApo objective. All image acquisition was performed using CellVoyager software (Yokogawa Electric Corporation).

Embryonic lethality scoring

Embryonic lethality and larval defects were scored in the post-run 10× scanned fields (16 fields per well). Hatched worms and unhatched embryos were counted for each well. All unhatched embryos were scored as embryonic lethal, with the exception of arrested one- to four-cell-stage embryos, which were excluded from the count because we observed that embryos dissected from control worms that emerge from the mothers before the end of meiosis II, when the eggshell permeability barrier forms, frequently arrest before the four-cell stage owing to osmotic complications during the first two divisions. To circumvent this issue, we also avoided the transfer of one-cell-stage embryos into the imaging wells, which reduced the possibility of including embryos with partially formed eggshells. Partially hatched or fully hatched worms with body morphology or behavioral defects, such as dumpy or paralyzed, were scored as 'abnormal larva'. Embryonic lethality was assessed for controls in each run. In the rare event that embryonic lethality in control wells exceeded 20% lethality (two s.d. from the mean for embryonic lethality percentage) the RNAi conditions for that run were repeated.

Automated cropping

Our automated cropping software, with straightforward instructions for setting it up on a PC or Mac, can be downloaded from zenodo.org/record/1475442#.W9jvApNKiUl (Wang et al., 2018), along with the source code repository for the GUI, which also includes Python code that can crop embryos from larger data sets in batch format (github.com/renatkh/embryo_crop.git). Our automated cropping software detects individual embryos in a binary mask, generated from the bright-field images, sequentially crops them out, and orients each embryo (Fig. 4C). Before cropping, the software corrects for drift, subtracts background and performs depth attenuation correction in each fluorescence channel (customizable options selectable in the GUI). Each step is described in detail below.

Drift was calculated by applying a phase correlation method to the central plane bright-field images; if calculated displacement between consecutive images was larger than 50 pixels, the correction was rejected. Background subtraction was performed on every image in every channel independently by applying a Gaussian filter (201 and 41-pixel sizes, respectively, for Morphogenesis strain and Germ Layer strain embryos) and subtracting the obtained background from the original image. Signal attenuation was corrected assuming a linear decay to 10% of signal strength within the 36 µm depth; these values were empirically determined.

Binary masks for cropping are generated from 8-bit bright-field images using the following steps: (1) bright-field images from a single *z*-stack are blurred using a Gaussian filter (sigma=11 pixels); (2) edges are detected using a Canny edge detection algorithm (Canny, 1986; high threshold set to 100, low threshold set to 30); (3) a maximum intensity projection is calculated from the three central planes of the edge-detected *z*-stack; (4) the resulting image is transformed with a closing morphology transformation (11 pixel size); (5) holes smaller than 2000 square pixels are filled in and objects less than 10,000 square pixels are removed from the mask.

Individual embryos are detected by fitting a Cassini oval to a section of the binary mask outline (Fig. 4C, Fig. S4G) using the following procedure: 100 arcs are extended in both directions from random seed points on the mask surface. An arc is allowed to extend only until the maximum indentation point between the arc and the shortest convex path that encases the entire arc (α in Fig. S4G) is >30 pixels; arc extension is also terminated if the distance between the point of divergence of the arc from the convex path and the point at which the arc and convex path re-converge (β in Fig. S4G) is greater than 30 pixels (i.e. if there is a long shallow indentation). When arc extension is terminated, the point of maximum indentation becomes the arc end. The arcs are extended to a maximum length of 1000 pixels. Each of the obtained arcs is fit to a Cassini oval and the oval with dimensions closest to 180×90 pixels is kept. This oval is cropped out from the mask, and the remaining mask is subjected to an open morphology transformation with a size of 11 pixels. Embryo detection and removal is repeated until the remaining mask has no objects larger than 10,000 square pixels. Individual image files for each embryo were assembled into composite movies for each condition using a custom ImageJ script (zenodo.org/record/1475442#.W9jvApNKiUl; Wang et al., 2018).

Anterior-posterior orientation

The anterior-posterior orientation of each embryo was determined using maximum intensity projections of the signal in the red channel after attenuation correction as illustrated in Fig. 4D. The ratio between the total fluorescence signal in the two halves of the embryos was calculated for three timepoints, corresponding to image frames 6, 8 and 10 for the Morphogenesis strain and 8, 10, and 12 for the Germ Layer strain, and embryos were oriented so that the average value of ratio of the fluorescence on the left side of the embryo to the average fluorescence on the right side of the embryo was greater than 1 (see schematic in Fig. 4D). If the ratio was less than one, the embryo was flipped. For the Germ Layer strain, if the ratio was between 0.8 and 1.25, we calculated the ratio for the red fluorescence after subtracting green fluorescence intensity, and required this ratio (left/right) to be >1.

Manual analysis of phenotypes

Movies were generated for each RNAi condition (available at datadryad.org/resource/doi:10.5061/dryad.kb79121; Wang et al., 2019) using a custom FIJI script that combined the cropped sequences for individual embryos (available at zenodo.org/record/1475442#.W9jvApNKiUl; Wang et al., 2018). Processed and assembled images were scored for a collection of 18 specific defects as described in the text. For details on how each defect was scored see Fig. S4 and Table S2.2. Some defects were scored in both strains and other defects were only scored in the Germ Layer or Morphogenesis strains. For a comparison of scored phenotypes with a summary of the expected phenotypes that are reported in Wormbase, see Expected-Observed Phenotypes tab in Table S2. For the arrest point analysis in Fig. 3E-F, the most prominent arrest point that was observed in at least two embryos was selected for each RNAi condition. If embryonic lethality counts were higher than 20% but no arrest point at the 3-fold stage or earlier emerged, the condition was marked as 'Other (EMB)'. If no phenotype was observed, but the RNAi condition scored above 20% abnormal larva, the condition was marked as 'larval abnormal'. If none of these criteria were met, the condition was marked as wild type.

Nuclear counts

To measure the total number of nuclei for each germ layer (Fig. 5B), the Batch Coordinator x64 tool in Imaris (Bitplane) was used to segment the nuclear signal in the 4D image stacks of individually cropped embryos and partition identified nuclei between red, green and yellow channels. To do this, we used an estimated nuclear diameter of 5 µm to define 'spots' for each channel. Nuclei were assigned to the red, green or yellow channels using the following intensity gate settings: green (green>7830 and red<6695); red (red>6695 and green<7830); and yellow (red>6695 and green>7830). This allowed for tracking of nuclear counts for each germ layer at each time point. Because nuclear count data is not accurate once

muscle contraction has initiated (owing to rapid movement of the worm inside the eggshell), we averaged nuclear count information for the three timepoints before the onset of movement; at this time (comma- to 2-fold-stage) the majority of cell divisions have been completed and cell fate has been specified. For conditions that exhibited an arrest before the onset of movement, the nuclear counts for the final three imaged timepoints were averaged. For the graph in Fig. 5B, the average nuclear count values for green, red and yellow nuclei in controls were subtracted from the values that were measured for each RNAi condition before plotting.

Competing interests

The authors declare no competing or financial interests.

Author contributions

Conceptualization: A.D., K.O., R.A.G.; Methodology: S.W., S.D.O., R.N.K., A.G.-G., A.D., A.D.C., K.O., R.A.G.; Software: R.N.K., R.A.G.; Formal analysis: S.D.O., J.M.H., Z.Z., R.N.K., R.A.G.; Investigation: S.W., S.D.O., A.G.-G., Z.Z., R.B., R.A.G.; Resources: A.D., K.O.; Data curation: S.D.O., J.M.H., R.N.K., R.A.G.; Writing - original draft: S.W., R.N.K., K.O., R.A.G.; Writing - review & editing: S.W., S.D.O., R.N.K., A.D.C., A.D., K.O., R.A.G.; Visualization: S.W., R.N.K., K.O., R.A.G.; Supervision: K.O., R.A.G.; Project administration: A.D., K.O., R.A.G.; Funding acquisition: A.D., K.O.

Funding

S.D.O. was supported by the National Institute of General Medical Sciences-sponsored University of California San Diego Institutional Research and Academic Career Development Award (NIH/IRACDA K12 GM068524) and A.D.C. was supported by the National Institutes of Health (R01 GM054657). A.D. and K.O. were supported by the Ludwig Institute for Cancer Research, which also provided them with research funding used to support this work. Deposited in PMC for release after 12 months.

Data availability

Data are available from the Dryad Digital Repository (Wang et al., 2019): dryad.kb79121. The automated cropping software can be downloaded from zenodo.org/record/1475442#.W9jvApNKiUl (Wang et al., 2018). The source code for the GUI can be downloaded from github.com/renatkh/embryo_crop.git.

Supplementary information

Supplementary information available online at
http://dev.biologists.org/lookup/doi/10.1242/dev.174029.supplemental

References

Ajuh, P., Kuster, B., Panov, K., Zomerdijk, J. C. B. M., Mann, M. and Lamond, A. I. (2000). Functional analysis of the human CDC5L complex and identification of its components by mass spectrometry. *EMBO J.* **19**, 6569-6581.

Ajuh, P., Sleeman, J., Chusainow, J. and Lamond, A. I. (2001). A direct interaction between the carboxyl-terminal region of CDC5L and the WD40 domain of PLRG1 is essential for pre-mRNA splicing. *J. Biol. Chem.* **276**, 42370-42381.

Altun, Z. F. and Hall, D. H. (2009). Epithelial system, interfacial cells. In *WormAtlas* (ed. L. A. Herndon). doi:10.3908/wormatlas.1.15.

Amin, N. M., Shi, H. and Liu, J. (2010). The FoxF/FoxC factor LET-381 directly regulates both cell fate specification and cell differentiation in C. elegans mesoderm development. *Development* **137**, 1451-1460.

Armenti, S. T. and Nance, J. (2012). Adherens junctions in C. elegans embryonic morphogenesis. *Subcell. Biochem.* **60**, 279-299.

Aspöck, G. and Burglin, T. R. (2001). The Caenorhabditis elegans distal-less ortholog ceh-43 is required for development of the anterior hypodermis. *Dev. Dyn.* **222**, 403-409.

Audhya, A., Hyndman, F., McLeod, I. X., Maddox, A. S., Yates, J. R., III, Desai, A. and Oegema, K. (2005). A complex containing the Sm protein CAR-1 and the RNA helicase CGH-1 is required for embryonic cytokinesis in Caenorhabditis elegans. *J. Cell Biol.* **171**, 267-279.

Bao, Z., Murray, J. I., Boyle, T., Ooi, S. L., Sandel, M. J. and Waterston, R. H. (2006). Automated cell lineage tracing in Caenorhabditis elegans. *Proc. Natl. Acad. Sci. USA* **103**, 2707-2712.

Canny, J. (1986). A computational approach to edge detection. *IEEE Trans. Pattern Anal. Machine Intell.* **8**, 679-698.

Chisholm, A. D. and Hardin, J. (2005). Epidermal morphogenesis. In *WormBook* (ed.The C. elegans Research Community), doi:10.1895/wormbook.1.35.1.

Chisholm, A. D. and Hsiao, T. I. (2012). The Caenorhabditis elegans epidermis as a model skin. I: development, patterning, and growth. *Wiley Interdiscip. Rev. Dev. Biol.* **1**, 861-878.

Christensen, R. P., Bokinsky, A., Santella, A., Wu, Y., Marquina-Solis, J., Guo, M., Kovacevic, I., Kumar, A., Winter, P. W., Tashakkori, N. et al. (2015). Untwisting the Caenorhabditis elegans embryo. *eLife* **4**, e10070.

Ding, M., Goncharov, A., Jin, Y. and Chisholm, A. D. (2003). C. elegans ankyrin repeat protein VAB-19 is a component of epidermal attachment structures and is essential for epidermal morphogenesis. *Development* **130**, 5791-5801.

Draper, B. W., Mello, C. C., Bowerman, B., Hardin, J. and Priess, J. R. (1996). MEX-3 is a KH domain protein that regulates blastomere identity in early C. elegans embryos. *Cell* **87**, 205-216.

Du, Z., Santella, A., He, F., Tiongson, M. and Bao, Z. (2014). De novo inference of systems-level mechanistic models of development from live-imaging-based phenotype analysis. *Cell* **156**, 359-372.

Du, Z., He, F., Yu, Z., Bowerman, B. and Bao, Z. (2015). E3 ubiquitin ligases promote progression of differentiation during C. elegans embryogenesis. *Dev. Biol.* **398**, 267-279.

Fakhouri, T. H. I., Stevenson, J., Chisholm, A. D. and Mango, S. E. (2010). Dynamic chromatin organization during foregut development mediated by the organ selector gene PHA-4/FoxA. *PLoS Genet.* **6**, e1001060.

Frøkjaer-Jensen, C., Davis, M. W., Hopkins, C. E., Newman, B. J., Thummel, J. M., Olesen, S. P., Grunnet, M. and Jorgensen, E. M. (2008). Single-copy insertion of transgenes in Caenorhabditis elegans. *Nat Genet.* **11**, 1375-1383.

Gally, C., Wissler, F., Zahreddine, H., Quintin, S., Landmann, F. and Labouesse, M. (2009). Myosin II regulation during C. elegans embryonic elongation: LET-502/ROCK, MRCK-1 and PAK-1, three kinases with different roles. *Development* **136**, 3109-3119.

Gilleard, J. S. and McGhee, J. D. (2001). Activation of hypodermal differentiation in the Caenorhabditis elegans embryo by GATA transcription factors ELT-1 and ELT-3. *Mol. Cell. Biol.* **21**, 2533-2544.

Giurumescu, C. A., Kang, S., Planchon, T. A., Betzig, E., Bloomekatz, J., Yelon, D., Cosman, P. and Chisholm, A. D. (2012). Quantitative semi-automated analysis of morphogenesis with single-cell resolution in complex embryos. *Development* **139**, 4271-4279.

Greenwald, I. and Kovall, R. (2013). Notch signaling: genetics and structure. In *WormBook* (ed.The C. elegans Research Community), doi:10.1895/wormbook.1.10.2.

Hall, B. K. (1999). *Evolutionary Developmental Biology*, Vol. XVIII, 491pp. Springer Netherlands.

Hallam, S., Singer, E., Waring, D. and Jin, Y. (2000). The C. elegans NeuroD homolog cnd-1 functions in multiple aspects of motor neuron fate specification. *Development* **127**, 4239-4252.

Hashimshony, T., Feder, M., Levin, M., Hall, B. K. and Yanai, I. (2015). Spatiotemporal transcriptomics reveals the evolutionary history of the endoderm germ layer. *Nature* **519**, 219-222.

Heid, P. J., Raich, W. B., Smith, R., Mohler, W. A., Simokat, K., Gendreau, S. B., Rothman, J. H. and Hardin, J. (2001). The zinc finger protein DIE-1 is required for late events during epithelial cell rearrangement in C. elegans. *Dev. Biol.* **236**, 165-180.

Ho, V. W. S., Wong, M.-K., An, X., Guan, D., Shao, J., Ng, H. C. K., Ren, X., He, K., Liao, J., Ang, Y. et al. (2015). Systems-level quantification of division timing reveals a common genetic architecture controlling asynchrony and fate asymmetry. *Mol. Syst. Biol.* **11**, 814.

Hunter, C. P. and Kenyon, C. (1996). Spatial and temporal controls target pal-1 blastomere-specification activity to a single blastomere lineage in C. elegans embryos. *Cell* **87**, 217-226.

Jackson, B. M. and Eisenmann, D. M. (2012). beta-catenin-dependent Wnt signaling in C. elegans: teaching an old dog a new trick. *Cold Spring Harb. Perspect. Biol.* **4**, a007948.

Krause, M., Harrison, S. W., Xu, S.-Q., Chen, L. and Fire, A. (1994). Elements regulating cell- and stage-specific expression of the C. elegans MyoD family homolog hlh-1. *Dev. Biol.* **166**, 133-148.

Kuersten, S. and Goodwin, E. B. (2003). The power of the 3′ UTR: translational control and development. *Nat. Rev. Genet.* **4**, 626-637.

Lamkin, E. R. and Heiman, M. G. (2017). Coordinated morphogenesis of neurons and glia. *Curr. Opin. Neurobiol.* **47**, 58-64.

Levin, M., Hashimshony, T., Wagner, F. and Yanai, I. (2012). Developmental milestones punctuate gene expression in the Caenorhabditis embryo. *Dev. Cell* **22**, 1101-1108.

Loveless, T. and Hardin, J. (2012). Cadherin complexity: recent insights into cadherin superfamily function in C. elegans. *Curr. Opin. Cell Biol.* **24**, 695-701.

Mango, S. E. (2007). The C. elegans pharynx: a model for organogenesis. In *WormBook* (ed.The C. elegans Research Community), doi:10.1895/wormbook.1.129.1.

Mazet, F., Amemiya, C. T. and Shimeld, S. M. (2006). An ancient Fox gene cluster in bilaterian animals. *Curr. Biol.* **16**, R314-R316.

Murray, J. I., Bao, Z., Boyle, T. J., Boeck, M. E., Mericle, B. L., Nicholas, T. J., Zhao, Z., Sandel, M. J. and Waterston, R. H. (2008). Automated analysis of embryonic gene expression with cellular resolution in C. elegans. *Nat. Methods* **5**, 703-709.

Murray, J. I., Boyle, T. J., Preston, E., Vafeados, D., Mericle, B., Weisdepp, P., Zhao, Z., Bao, Z., Boeck, M. and Waterston, R. H. (2012). Multidimensional regulation of gene expression in the C. elegans embryo. *Genome Res.* **22**, 1282-1294.

Nance, J. and Priess, J. R. (2002). Cell polarity and gastrulation in C. elegans. *Development* **129**, 387-397.
Nishi, Y., Rogers, E., Robertson, S. M. and Lin, R. (2008). Polo kinases regulate C. elegans embryonic polarity via binding to DYRK2-primed MEX-5 and MEX-6. *Development* **135**, 687-697.
Pagano, J. M., Farley, B. M., Essien, K. I. and Ryder, S. P. (2009). RNA recognition by the embryonic cell fate determinant and germline totipotency factor MEX-3. *Proc. Natl. Acad. Sci. USA* **106**, 20252-20257.
Page, B. D., Zhang, W., Steward, K., Blumenthal, T. and Priess, J. R. (1997). ELT-1, a GATA-like transcription factor, is required for epidermal cell fates in Caenorhabditis elegans embryos. *Genes Dev.* **11**, 1651-1661.
Panganiban, G. and Rubenstein, J. L. (2002). Developmental functions of the Distal-less/Dlx homeobox genes. *Development* **129**, 4371-4386.
Patel, F. B., Bernadskaya, Y. Y., Chen, E., Jobanputra, A., Pooladi, Z., Freeman, K. L., Gally, C., Mohler, W. A. and Soto, M. C. (2008). The WAVE/SCAR complex promotes polarized cell movements and actin enrichment in epithelia during C. elegans embryogenesis. *Dev. Biol.* **324**, 297-309.
Pauli, F., Liu, Y., Kim, Y. A., Chen, P. J. and Kim, S. K. (2006). Chromosomal clustering and GATA transcriptional regulation of intestine-expressed genes in C. elegans. *Development* **133**, 287-295.
Pollard, T. D. (2017). What we know and do not know about actin. *Handb. Exp. Pharmacol.* **235**, 331-347.
Powell-Coffman, J. A., Knight, J. and Wood, W. B. (1996). Onset of C. elegans gastrulation is blocked by inhibition of embryonic transcription with an RNA polymerase antisense RNA. *Dev. Biol.* **178**, 472-483.
Priess, J. R. (2005). Notch signaling in the C. elegans embryo. In *WormBook* (ed.The C. elegans Research Community), doi:10.1895/wormbook.1.4.1.
Rasmussen, J. P., Feldman, J. L., Reddy, S. S. and Priess, J. R. (2013). Cell interactions and patterned intercalations shape and link epithelial tubes in C. elegans. *PLoS Genet.* **9**, e1003772.
Robertson, S. and Lin, R. (2015). The maternal-to-zygotic transition in C. elegans. *Curr. Top. Dev. Biol.* **113**, 1-42.
Santella, A., Du, Z., Nowotschin, S., Hadjantonakis, A.-K. and Bao, Z. (2010). A hybrid blob-slice model for accurate and efficient detection of fluorescence labeled nuclei in 3D. *BMC Bioinformatics* **11**, 580.
Sawa, H. and Korswagen, H. C. (2013). Wnt signaling in C. elegans. In *WormBook* (ed.The C. elegans Research Community), doi:10.1895/wormbook.1.7.2.
Sawa, M., Suetsugu, S., Sugimoto, A., Miki, H., Yamamoto, M. and Takenawa, T. (2003). Essential role of the C. elegans Arp2/3 complex in cell migration during ventral enclosure. *J. Cell Sci.* **116**, 1505-1518.
Schmitz, C., Kinge, P. and Hutter, H. (2007). Axon guidance genes identified in a large-scale RNAi screen using the RNAi-hypersensitive Caenorhabditis elegans strain nre-1(hd20) lin-15b(hd126). *Proc. Natl. Acad. Sci. USA* **104**, 834-839.
Schubert, C. M., Lin, R., de Vries, C. J., Plasterk, R. H. A. and Priess, J. R. (2000). MEX-5 and MEX-6 function to establish soma/germline asymmetry in early C. elegans embryos. *Mol. Cell* **5**, 671-682.
Shah, P. K., Tanner, M. R., Kovacevic, I., Rankin, A., Marshall, T. E., Noblett, N., Tran, N. N., Roenspies, T., Hung, J., Chen, Z. et al. (2017). PCP and SAX-3/Robo pathways cooperate to regulate convergent extension-based nerve cord assembly in C. elegans. *Dev. Cell* **41**, 195-203.e3.
Sheffield, M., Loveless, T., Hardin, J. and Pettitt, J. (2007). C. elegans Enabled exhibits novel interactions with N-WASP, Abl, and cell-cell junctions. *Curr. Biol.* **17**, 1791-1796.
Simmer, F., Moorman, C., van der Linden, A. M., Kuijk, E., van den Berghe, P. V. E., Kamath, R. S., Fraser, A. G., Ahringer, J. and Plasterk, R. H. A. (2003). Genome-wide RNAi of C. elegans using the hypersensitive rrf-3 strain reveals novel gene functions. *PLoS Biol.* **1**, e12.
Sjoqvist, M. and Andersson, E. R. (2017). Do as I say, Not(ch) as I do: lateral control of cell fate. *Dev. Biol.* **447**, 58-70.
Soto, M. C., Qadota, H., Kasuya, K., Inoue, M., Tsuboi, D., Mello, C. C. and Kaibuchi, K. (2002). The GEX-2 and GEX-3 proteins are required for tissue morphogenesis and cell migrations in C. elegans. *Genes Dev.* **16**, 620-632.
Spickard, E. A., Joshi, P. M. and Rothman, J. H. (2018). The multipotency-to-commitment transition in Caenorhabditis elegans-implications for reprogramming from cells to organs. *FEBS Lett.* **592**, 838-851.
Sullivan-Brown, J. L., Tandon, P., Bird, K. E., Dickinson, D. J., Tintori, S. C., Heppert, J. K., Meserve, J. H., Trogden, K. P., Orlowski, S. K., Conlon, F. L. et al. (2016). Identifying regulators of morphogenesis common to vertebrate neural tube closure and Caenorhabditis elegans gastrulation. *Genetics* **202**, 123-139.
Sulston, J. E., Schierenberg, E., White, J. G. and Thomson, J. N. (1983). The embryonic cell lineage of the nematode Caenorhabditis elegans. *Dev. Biol.* **100**, 64-119.
Vuong-Brender, T. T. K., Yang, X. and Labouesse, M. (2016). C. elegans embryonic morphogenesis. *Curr. Top. Dev. Biol.* **116**, 597-616.
Wang, J. T. and Seydoux, G. (2013). Germ cell specification. *Adv. Exp. Med. Biol.* **757**, 17-39.
Wang, S., Ochoa, S. D., Khaliullin, R. N., Gerson-Gurwitz, A., Hendel, J. M., Zhao, Z., Biggs, R., Chisholm, A., Desai, A., Oegema, K., Green, R. A. (2018). A high-content imaging method for monitoring C. elegans embryonic development. *Zenodo* doi:10.5281/zenodo.1475442.
Wang, S., Ochoa, S. D., Khaliullin, R. N., Gerson-Gurwitz, A., Hendel, J. M., Zhao, Z., Biggs, R., Chisholm, A., Desai, A., Oegema, K., Green, R. A. (2019). Data from: A high-content imaging method for monitoring C. elegans embryonic development. *Dryad Digital Repository* doi:10.5061/dryad.kb79121.
Wissmann, A., Ingles, J., McGhee, J. D. and Mains, P. E. (1997). Caenorhabditis elegans LET-502 is related to Rho-binding kinases and human myotonic dystrophy kinase and interacts genetically with a homolog of the regulatory subunit of smooth muscle myosin phosphatase to affect cell shape. *Genes Dev.* **11**, 409-422.
Wissmann, A., Ingles, J. and Mains, P. E. (1999). The Caenorhabditis elegans mel-11 myosin phosphatase regulatory subunit affects tissue contraction in the somatic gonad and the embryonic epidermis and genetically interacts with the Rac signaling pathway. *Dev. Biol.* **209**, 111-127.
Wolpert, L., Tickle, C. and Arias, A. M. (2015). *Principles of Development*. Oxford University Press.
Zhang, H. and Labouesse, M. (2010). The making of hemidesmosome structures in vivo. *Dev. Dyn.* **239**, 1465-1476.
Zhong, M., Niu, W., Lu, Z. J., Sarov, M., Murray, J. I., Janette, J., Raha, D., Sheaffer, K. L., Lam, H. Y. K., Preston, E. et al. (2010). Genome-wide identification of binding sites defines distinct functions for Caenorhabditis elegans PHA-4/FOXA in development and environmental response. *PLoS Genet.* **6**, e1000848.